Available online at www.sciencedirect.com
SCIENCE DIRECT®
International Journal of Heat and Fluid Flow 25 (2004) 431–443
International Journal of HEAT AND FLUID FLOW
www.elsevier.com/locate/ijhff

Direct numerical simulation of momentum and heat transport in idealized Czochralski crystal growth configurations

Claus Wagner [a,*], R. Friedrich [b]

[a] Institute for Aerodynamics and Flow Technology, German Aerospace Center, 37073 Göttingen, Germany
[b] Fachgebiet Strömungsmechanik, Munich University of Technology, 85748 Garching, Germany

Abstract

Turbulent momentum and heat transport in idealized Czochralski crystal growth configurations is investigated by means of direct numerical simulation. The analysis of the flow data focuses on the influence of crystal and crucible rotation on the flow structures and the development of temperature fluctuations. A numerical parameter study is performed to investigate how the variation of the numerous flow parameters affects the turbulent transport processes. Finally, a direct numerical simulation is conducted with parameters taken from experiment in order to allow a direct comparison between numerical and experimental results. It is found that counter-rotation of the crystal and crucible leads to a complex flow, which is characterized by three major recirculation zones, if crucible rotation dominates the flow. The dynamics of the flow are controlled by centrifugal forces counteracting buoyancy and surface tension effects. High temperature fluctuations are created within or close to the crystallization zone. Neither a variation of the melt height, nor a reduction of the crystal rotation rate or a change of the Grashof and Marangoni numbers has a major effect on the bulk flow structure and overall heat transfer. Increasing rotation of the crystal changes the bulk flow structure strongly and leads to an increased value of maximum rms temperature fluctuations, the position of which is shifted towards the crucible bottom. A shifted position of maximum rms temperature fluctuations is also observed if heat radiation across the free surface is taken into account.

Keywords: Czochralski crystal growth configuration; Direct numerical simulation; Temperature fluctuation; Turbulence structure

1. Introduction

Semiconductor industry has a high demand for pure silicon crystal, which is needed to produce all sorts of electronical devices. Around 90% of the worldwide silicon demand is grown utilizing the Czochralski process. In Czochralski crystal growth configurations the low Prandtl number silicon melt is kept in a cylindrical crucible. Heating the crucible side wall gives rise to buoyant convection. The crystal is pulled from the free surface at rates between a few millimeters to centimeters per second. Along the free surface, Marangoni convection develops due to radial temperature gradients between the side wall and the comparably cold cylindrical crystal. Crucible and crystal are commonly rotated in opposite directions, so that centrifugal forces counteract buoyancy and surface-tension driven convection. In addition, thermal conduction and heat radiation at the free surface induce losses of heat to the surrounding.

The fluid flow and heat transfer processes in the melt of a Czochralski growth system are extremely complex, since several effects arise simultaneously in this process. Among the associated instabilities are the Rayleigh–Bénard, baroclinic and Küppers–Lortz instabilities. They lead to time-dependent three-dimensional motions in the melt, which influence the transport of dopant, impurities and heat to the crystal/melt interface and thus determine the purity of the crystal.

That the Czochralski melt flow is turbulent, has been already suspected about thirty years ago by Wilcox and Fullmer (1965) who used thermocouples to measure temperature fluctuations in a calcium fluoride melt (with a *Pr* number of the order of 1 (O[1]) confined in a rather

* Corresponding author. Address: DLR Gottingen, Inst. für Stromungsmechanik, Bunsenstr. 10, 37073 Göttingen, Germany. Tel.: +49-551-709-2261; fax: +49-551-709-2446.
E-mail addresses: claus.wagner@dlr.de (C. Wagner), r.friedrich@lrz.tu-muenchen.de (R. Friedrich).

0142-727X/$ - see front matter © 2004 Elsevier Inc. All rights reserved.
doi:10.1016/j.ijheatfluidflow.2004.02.023

Nomenclature

$\vec{b}$	buoyancy vector
c	capillary coefficient
g	gravitational acceleration
Gr	Grashof number
Ma	Marangoni number
p	pressure
Pr	Prandtl number
r	radial coordinate
R	radius
Re	Reynolds number based on U_b, D
$\vec{u}$	velocity vector
u_b	buoyancy velocity scale
u_z, u_φ, u_r	velocity components in axial, circumferential, radial direction
z	axial coordinate

Greeks

α	thermal expansion coefficient
λ	thermal conductivity
φ	azimuthal coordinate
σ	radiation constant
ρ	density
ε	dissipation rate
ε_h	emission coefficient
γ	thermal diffusivity
ν	kinematic viscosity
ω	rotational frequency

Other symbols

$\langle \cdot\cdot \rangle$	Reynolds average
$(\cdot\cdot)'$	fluctuation
$(\cdot\cdot)_s$	notation for crystal
$(\cdot\cdot)_c$	notation for crucible
∇	gradient
∇^2	Laplacian

small crucible ($Gr = 10^6$). Most of the experimental investigations alluding to the fluctuating nature of the flow have been done in rather small melt volumes of too high Prandtl number. One reason for that might be that the experimental investigation of these low Prandtl number turbulent flow and heat transport processes faces lots of difficulties. In large scale growth systems the flow is mostly turbulent, the melts are usually opaque and due to their high freezing temperature unsuitable for most tracer particles.

The convection of a transparent fluid (Prandtl number O[1]) forced by rotation of the crystal in a non-rotating heated crucible was investigated in the experiment of Jones (1989). In the vicinity of the crystal he observed temperature fluctuations of high amplitude. From temperature measurements by Kuroda et al. (1982) it is known that temperature fluctuations of large amplitude are responsible for an increased concentration of microdefects in the crystal.

For the low Grashof number regime there have been a number of time-dependent two and three-dimensional numerical simulations of Czochralski melt flow. Mihelcic et al. (1984) were among the first to attempt three-dimensional simulations studying the bulk flow structure and transition from a two to three-dimensional flow state. Bottaro and Zebib (1989) simulated the three-dimensional time-dependent buoyant flow in a cylindrical confinement without taking the rotation of the crucible and crystal into account. Also in a vertical cylinder heated from below Wagner et al. (1994) computed critical thresholds for the breakdown of axisymmetry in surface-tension and buoyancy driven flows. For an aspect ratio (height to radius) of 1 and a Prandtl number of $Pr = 6.7$ they observed a direct transition from the quiescent state to a three-dimensional surface-driven flow state.

Later Xiao and Derby (1995) performed numerical simulations to focus on the three-dimensional oscillatory state of the Czochralski flow for a high Prandtl number fluid ($Pr = 8$). A bulk-flow model is applied to compute the flow for a Grashof number $Gr = 2.5 \times 10^5$ with a Galerkin finite element method. Investigating the transition from axisymmetric to non-axisymmetric flow states they observe a strong influence on the temperature distribution and heat transfer through the melt.

Recently Vizman et al. (2001) reported temperature measurements at different locations within a silicon melt kept in a small industrial Czochralski crucible of radius $R_c = 0.17$ m. For the same configuration Enger et al. (2001) performed marginally resolved numerical simulations on structured but curvilinear grids for Grashof numbers up to $Gr = 10^9$. They showed that their simulated temperature data agree fairly well with the temperature measurements of Vizman et al. (2001).

It is the aim of this work to investigate the influence that varying rotation rates of crucible and crystal, heat radiation at the free surface, different melt heights and crucible dimensions have on the development of temperature fluctuations at high Grashof numbers ranging from 1.0×10^8 to 2.0×10^9. This is done by means of Direct Numerical Simulation on cylindrical grids with up to 4.5 million grid points. In this study the Czochralski configuration is idealized in the sense that a flat free surface and a flat crystal/melt interface are assumed.

2. Numerical method

The incompressible Navier–Stokes equations in Boussinesq approximation

$$\nabla \cdot \vec{u} = 0 \tag{1}$$

$$\partial\vec{u}/\partial t + \nabla \cdot (\vec{u}\vec{u}) = -\nabla p + \nabla^2\vec{u}/Gr + \vec{b} \tag{2}$$

$$\partial u/\partial t = -(\vec{u} \cdot \nabla)T + \nabla^2 T/(Pr\sqrt{Gr}) \tag{3}$$

are integrated applying Schumann's volume balance procedure (Schumann, 1973) in cylindrical coordinates. The nabla operator ∇ and the velocity vector $\vec{u} = (u_z, u_\varphi, u_r)$ in Eqs. (1)–(3) are non-dimensionalized with the crucible radius R_c and the buoyancy velocity scale $u_b = (\alpha g R_c(T_c - T_s))^{1/2}$. A dimensionless temperature is defined by $(2T - (T_c + T_s))/(2(T_c - T_s))$. $\vec{b}$ represents the dimensionless buoyancy vector. The pressure p and time t are made dimensionless with ρ_b and R_c/u_b, respectively.

The Grashof number $Gr = (\alpha g R_c^3(T_c - T_s))/\nu^2$ and the Prandtl number $Pr = \nu/\gamma = 0.0175$ contain the thermal expansion coefficient $\alpha = 10^{-4}$ 1/K, the kinematic viscosity $\nu = 3.12 \times 10^{-7}$ m^2/s, the thermal conductivity γ and the gravitational acceleration g. Their values are those of a Si-melt.

Integrating Eqs. (1)–(3) provides a set of spatially discrete equations on staggered grids. Utilizing second order central interpolation and differentiation schemes leads to a method which is suitable for DNS. Within a second order semi-implicit time integration scheme all convection/diffusion terms of the momentum equations containing derivatives in circumferential direction as well as all diffusive terms of the heat conduction equation are integrated implicitly by a Crank-Nicholson time step. The remaining convection terms are treated explicitly with a Leapfrog time step, which is restricted by a linear stability criterion.

A fractional step approach provides the oscillation-free coupling between pressure and velocity fields and leads to a three dimensional Poisson equation for the pressure correction, which has to be solved at each time step. A 3D-Helmholtz equation has to be solved due to the implicit treatment of the temperature. The direct solutions of these elliptic equations are obtained using FFTs in φ-direction and cyclic reduction algorithms for the remaining 2D Helmholtz problems. The 1D Helmholtz problems associated with the implicit treatment of the φ-derivatives in the momentum equations are solved by a tridiagonal matrix algorithm.

3. Boundary conditions and geometrical outline

The cylindrical computational domain is presented in Fig. 1. A crystal of radius R_s, the axis of which coincides with the axis of the cylindrical crucible, grows out of a melt of height H at the free surface. The freezing temperature of silicone (1485 K) defines the dimensionless crystal temperature $T_s = -0.5$. Heating at the crucible sidewall is modelled assuming a constant temperature $T_c = 0.5$ in most simulations. Boundary conditions at the side and bottom walls of the crucible and the interface to the crystal are the impermeability condition for the wall normal components and the no slip conditions for the tangential velocity components. The solid-body rotation of the crucible and the crystal are imposed on the circumferential velocity component at the crystal/melt and crucible-bottom/melt boundaries. Fixed temperature boundary conditions are specified at the side wall of the crucible and the crystal/melt interface. For most cases the bottom of the crucible and the free surface are assumed to be adiabatic. The flat free surface further forces the axial velocity component to vanish. Finally, at the free surface, shear and heat boundary conditions (4)–(6) are discretized.

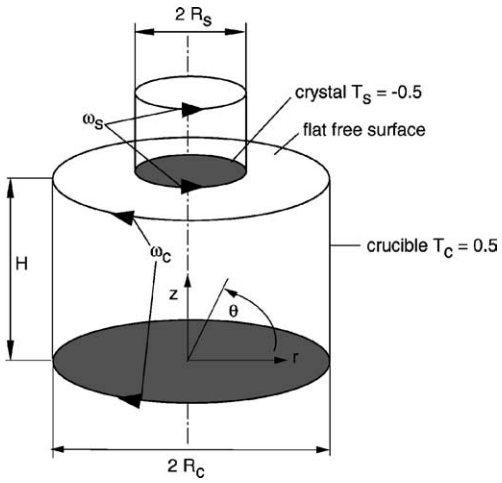

Fig. 1. Geometry of the Czochralski configuration.

$$\partial u_r/\partial z = -Ma/(Pr\sqrt{Gr})\partial T/\partial z \tag{4}$$

$$\partial u_\varphi/\partial z = -Ma/(Pr\sqrt{Gr})\partial T/(r\partial\varphi) \tag{5}$$

$$\partial T/\partial z = -(4R_c\varepsilon_h\sigma T_s^3/\lambda)T - \varepsilon_h\sigma R_c(T_s^4 - T_h^4)/(\lambda\Delta T) \tag{6}$$

In these equations $Ma = (cR_c(T_c - T_s))/\gamma$ defines the Marangoni number which contains the capillary coefficient $c = 0.149$ according the value for a Si-melt open to the ambient air. Furthermore, $\sigma = 5.75 \times 10^{-8}$ J/(s m^2 K^4) denotes the radiation constant, $\varepsilon_h = 0.23$ the emission coefficient, $\lambda = 46.6$ J/(s m K) the thermal conductivity and T_h the background temperature.

4. Results

The different flow parameters used in the direct numerical simulations (DNS) discussed below are

Table 1
Flow parameters and grid points of turbulent Czochralski flow simulations ($N_\varphi = 128$ in all cases)

DNS	1	2	3	4	5	6	7	8
N_z, N_r	196, 174	66, 92	66, 92	130, 130	196, 196	130, 130	130, 130	131, 174
Gr	10^8	10^8	10^8	10^8	10^9	10^8	10^8	1.6×10^9
Ma	36,000	36,000	36,000	36,000	70,000	36,000	5000	28,000
Re	4712	4712	76.7	20,950	14,902	4712	4712	16782
ω_c/ω_s	−0.7	−0.7	−43.0	−0.1	−0.7	−0.7	−0.7	−0.25
H/R_c	1.0	0.5	1.0	1.0	1.0	1.0	1.0	0.5

summarized in Table 1. The parameter combination of DNS_1 defines the reference case of a crucible with the radius $R_c = 4.8$ cm rotating at 16.8 rpm and having a temperature difference of $\Delta T = T_c - T_s = 91.4$ K. This leads to a Grashof number $Gr = 10^8$, a Marangoni number $Ma = 36000$ and a Reynolds number based on the angular frequency ω_s and the radius of the crystal of $Re = \omega_s R_s^2/\nu = 4712$. Furthermore, a rotation ratio $\omega_c/\omega_s = -0.7$ was specified. For all simulations grids with $N\varphi = 128$ points in φ-direction were used. Regarding the axial and radial directions the number of grid points N_z and N_r used are summarized in Table 1. With DNS_2–DNS_7 we study the influence of parameter variations on the turbulent momentum and heat transport comparing the results to those obtained in DNS_1. For DNS_1–DNS_7 the ratio between the crystal and crucible radius was fixed to $R_s/R_c = 0.5$. Solely for DNS_8, which was performed to compare our results to temperature measurements by Wacker Siltronic (2001), a ratio $R_s/R_c = 0.294$ was specified.

DNS_1 was started at $t = 0$ with the initial field

$$u_r = u_\varphi = u_z = 0, \quad T = T_c + T_{\text{random}} \tag{7}$$

where T_{random} stands for numerically created random temperature perturbations between −0.1 and 0.1. After the solution of DNS_1 reached a statistically steady state, an instantaneous flow field was interpolated on the other grids to define the initial turbulent fields for DNS_2-DNS_8. After each of the simulations reached a statistically steady state more than 1500 realizations with a time lag of 50 time steps (one time step corresponding to approximately 7×10^{-4} problem times R/u_b) were averaged in circumferential direction and in time to obtain stable statistical values.

4.1. Instantaneous fields

In a perspective view contours of the radial velocity component and of the temperature field which were calculated in DNS_1 are shown in Fig. 2 (left). Buoyancy drives the melt upwards along the heated crucible side wall as indicated by the wall parallel isotherms in this region (Fig. 2 (right)).

The flow turns inward at the meniscus and moves along the free surface creating a flow towards the cylinder axis. In the vicinity of the crystal the fluid encounters the outward flow driven by centrifugal effects due to crystal rotation. These two counteracting mechanisms lead to local ejections of cold fluid into the buoyancy driven hot recirculation zone, creating large amplitude temperature fluctuations there, as indicated by the dashed isotherms in the vicinity of the crystal

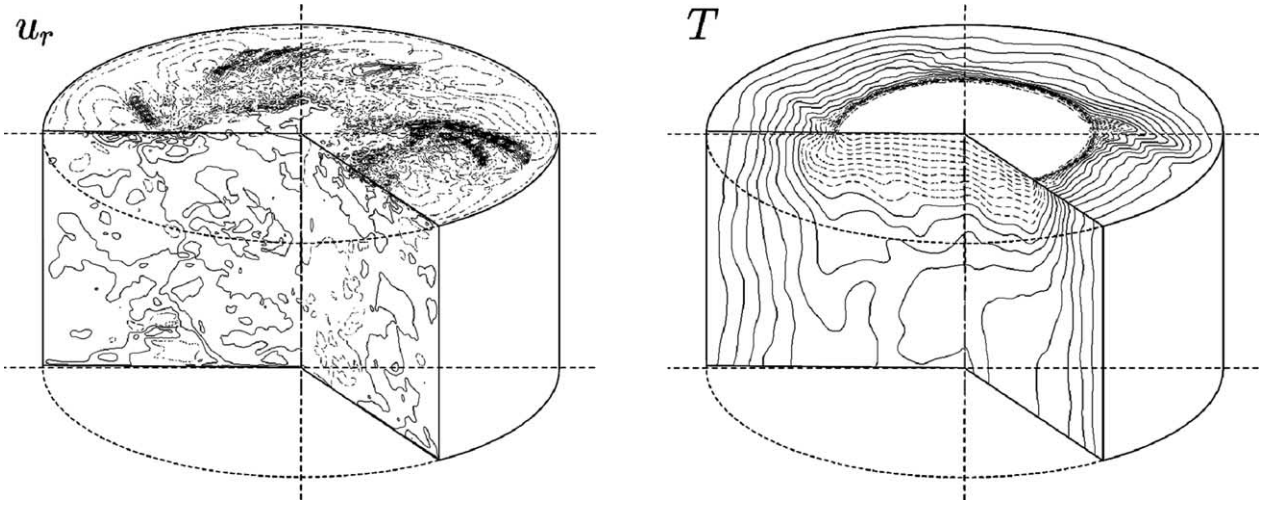

Fig. 2. Snapshot of the instantaneous radial velocity component u_r ($(u_r)_{max} = 1.497$, $(u_r)_{min} = -1.581$) and the instantaneous temperature T. Solid/dashed contour lines represent positive/negative values.

edge at the free surface in Fig. 2 (right). They are also visible in a cross-section at distance $0.01R_c$ from the free surface and are shown in Fig. 3, where contour lines of temperature fluctuations T' having amplitudes between -0.295 and 0.236 (see Fig. 3 (right)) are plotted.

4.2. Statistically averaged flow fields

Streamlines of the mean velocities in a (z,r)-plane in Fig. 4 (left) reveal four major recirculation zones for DNS_1. One of these cells develops underneath the crystal close to the bottom of the crucible, another one along the crucible wall, the third one just underneath the free surface and the crystal and a fourth one between the latter two. The contours of the circumferential velocity component, which dominates the momentum transport close to the crucible wall, are predominantly vertically oriented, as shown in Fig. 4 (right). Only in a thin layer along the bottom and top boundaries do the high gradients of the contours reflect a transport of melt with a low angular momentum towards the crucible wall at the bottom wall and of high angular momentum towards the crystal edge just below the free surface.

Similar to the instantaneous temperature field the isotherms of the mean temperature are vertically oriented near the side wall of the crucible as depicted in Fig. 5 (left). The cold fluid underneath the crystal is driven outward by the crystal rotation creating high temperature gradients when heated up by the fluid of the buoyancy driven recirculation zone. The mean isotherms underneath the crystal are aligned with the crystal/melt interface fulfilling a necessary condition for a vertically uniform crystal growth. Also beneficial for solidification is the encapsulation of cold fluid underneath the crystal since this prevents undercooling of the melt.

Contours of rms temperature fluctuations are presented in Fig. 5 (right). The position of the maximum rms temperature fluctuation is located within the crystallization zone close to the crystal edge with values of

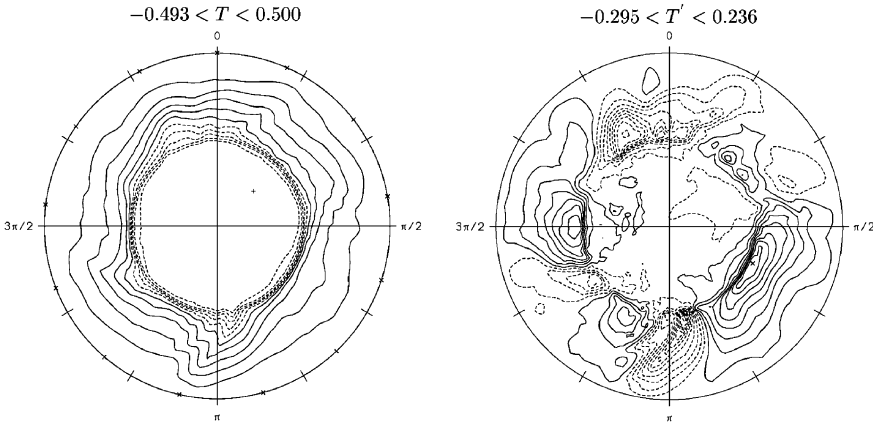

Fig. 3. Instantaneous (left) and fluctuating (right) isotherms in a cross-section (r,φ) located $0.01R_c$ below the free surface. Solid/dashed lines represent positive/negative and +/× minimum/maximum values.

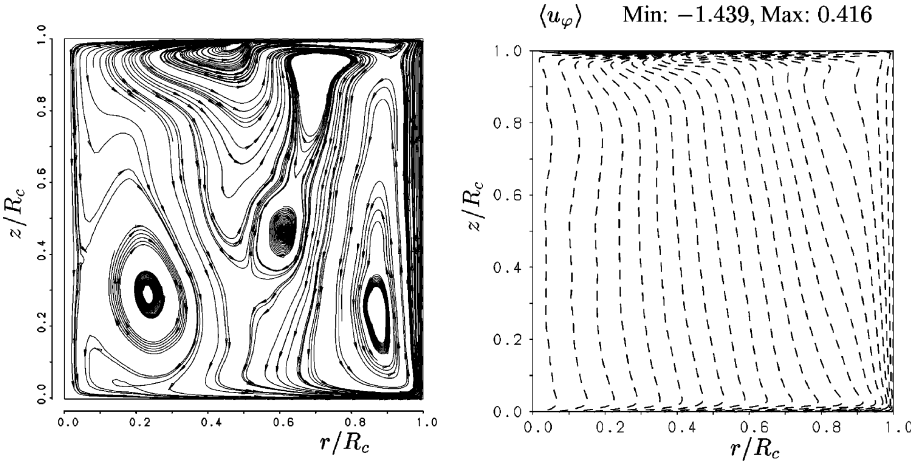

Fig. 4. Streamlines of the mean velocity fields (left) and contours of the circumferential velocity component (right) projected into (z,r)-planes of DNS_1 (reference case).

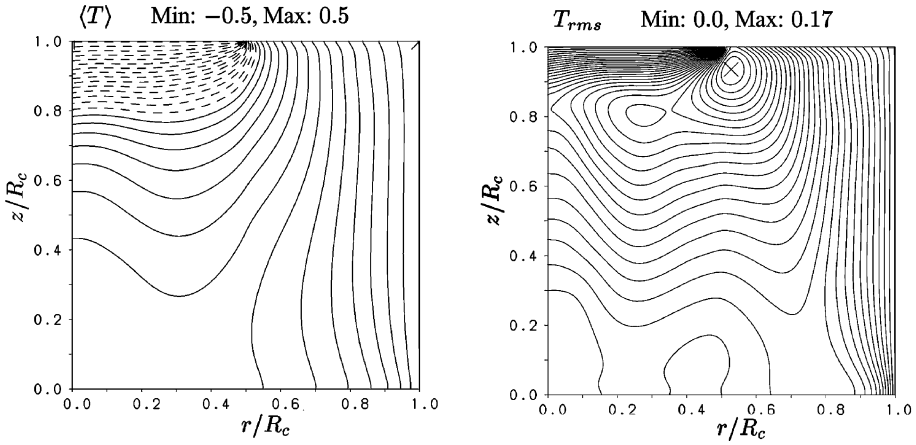

Fig. 5. Mean and rms-values of isotherms for DNS_1 (reference case). Solid/dashed lines represent positive/negative values.

$T_{\mathrm{rms}} = 0.17$ (≈15.4 K). Instantaneous temperature fluctuations even reach values of 28 K. These large temperature fluctuations are the most probable cause of micro-defects in the crystal.

The skewness of the temperature fluctuations (normalized with its variance) is a quantity which (unlike the skewness of the velocity fluctuations) does not appear in the transport equation of the temperature variance. However, it reveals the nature of the temperature fluctuations, i.e. it characterizes the frequency and size of the fluctuations above or below the local mean. At the crystal melt interface it indicates the extent of periods of

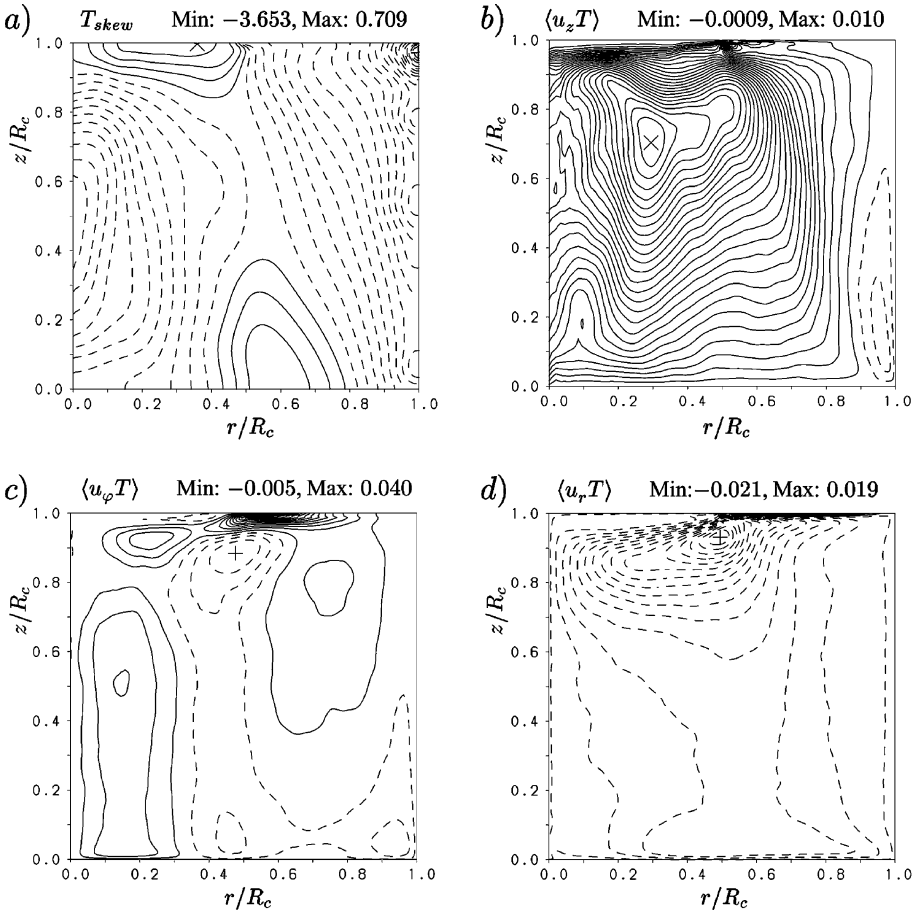

Fig. 6. Contours of the skewness of temperature fluctuations in (a) and components of the turbulent heat transport vector in axial, azimuthal and radial direction in (b–d). Solid/dashed lines represent positive/negative values and +/× denote minimal/maximal values.

rapid solidification or melt-back of the crystal interface. Fig. 6(a) contains contour lines of the temperature fluctuation's skewness in the case of counter-rotation of crystal and crucible.

Maximum positive fluctuations are observed immediately below the solid/liquid interface. The strong radial gradient of this quantity below the crystal can be expected to cause defects in the crystal.

The heat transport in axial direction in a plane containing the crucible axis, as plotted in Fig. 6(b), is positive in most parts of the domain. Only near the side wall, where the flow has boundary layer characteristics, it is negative, mainly due to production by the mean radial temperature gradient and by mean shear (which are the dominant mechanisms). The radial turbulent heat flux (Fig. 6(d)), on the other hand, transports heat from the sidewall to the core of the silicon melt. Similar effects (i.e. a heat transport against the flow direction and away from the wall) have also been observed in fully developed pipe flow by Lai and So (1990) and in supersonic boundary layers along adiabatic and cooled walls by LeRibault and Friedrich (1997) with the help of modelled transport equations for the turbulent heat fluxes. The circumferential heat transport due to turbulent motion in Fig. 6(c) reflects the effects of crystal and crucible rotation and has to be interpreted in connection with the mean streamlines (Fig. 4).

4.3. Spatial resolution requirements

An upper limit for the mean mesh size $h_{\min}$ of a DNS was derived by Grötzbach (1983) demanding that the Kolmogorov length scale $l_k = (\varepsilon/\nu^3)^{1/4}$ has to be resolved on the mesh.

$$h = (r\Delta\varphi\Delta r\Delta z)^{1/3} \leqslant \pi(\nu^3/\varepsilon)^{1/4} \quad \text{or} \quad h_{\min} = \pi/\varepsilon_{\max}^{1/4} Gr^{-3/8} \tag{8}$$

In Eq. (8) the dimensionless mean mesh size $h_{\min}$ depends on the Grashof number and the dimensionless dissipation rate ε, which is initially unknown. Evaluating ε using DNS_1-data, a maximum dissipation rate of $\varepsilon_{\max} = 0.377$, which peaks just underneath the crystal edge and a volume averaged value $\bar{\varepsilon} = 0.0066$ were obtained. Substituting $\varepsilon_{\max}$ into Eq. (8) leads to a mean mesh size $h_{\min} = 0.0044$. This must be compared to the mean mesh size of DNS_1, which varies from $h = 0.00277$ at the centerline to $h = 0.0108$ at the crucible side wall. Taking into account that the dissipation rate peaks underneath the crystal edge for $r/R_c = 0.5$ and that ε is considerably lower everywhere else in the flow, it is concluded that the grid is fine enough to resolve all the major physics.

4.4. Parameter study

The streamlines of the mean velocities in Fig. 7 reflect the flow in the case of smaller melt height (DNS_2), with the three major recirculation zones revealing similarities to the flow observed in DNS_1.

Although rotation rates of crucible and crystal are unchanged, the wetting surface at the crucible sidewall and consequently the influence of crucible rotation is reduced. This leads to a distribution of the circumferential velocity component which reflects two characteristic regions, one below the crystal, where the contours are predominantly vertically oriented, and a second one, below the free surface with transversal contours. As indicated by the dashed isotherms in Fig. 8 cold fluid extends over more than one half of the melt height, which indicates that the danger of cristallization of the melt increases for lower melt heights.

For the lower crystal rotation rate in DNS_3, streamlines of the mean velocity fields in Fig. 9 (left) and isotherms in Fig. 10 (left) show the same flow structure as presented in Figs. 7 and 8 for DNS_2. Even contours of rms temperature fluctuations of DNS_3 (lower melt height) in Fig. 8 (right) and of DNS_3 (smaller crystal rotation) in Fig. 10 (right) as well as the position of their maximum values agree remarkably well. On the other hand, lower crystal rotation rates and to some degree lower melt heights damp temperature fluctuations as indicated by the lower maximum $T_{\rm rms}$ in Figs. 8 (right) and 10 (right). Therefore, it is concluded that a decrease of crucible rotation with respect to the parameter combination of DNS_1 does not tremendously change the condition in the cristallization zone. Solely, the contours

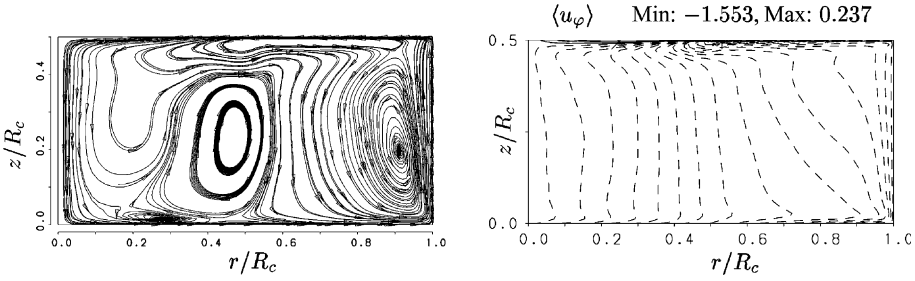

Fig. 7. Streamlines of the mean velocity fields (left) and contours of the circumferential velocity component (right) projected into (z, r)-planes of DNS_2 (low melt height).

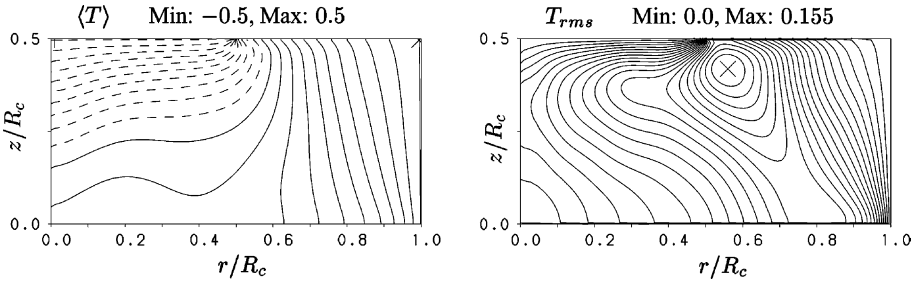

Fig. 8. Mean (left) and rms-values (right) of isotherms obtained in DNS_2 (low melt height). Solid/dashed lines represent positive/negative values.

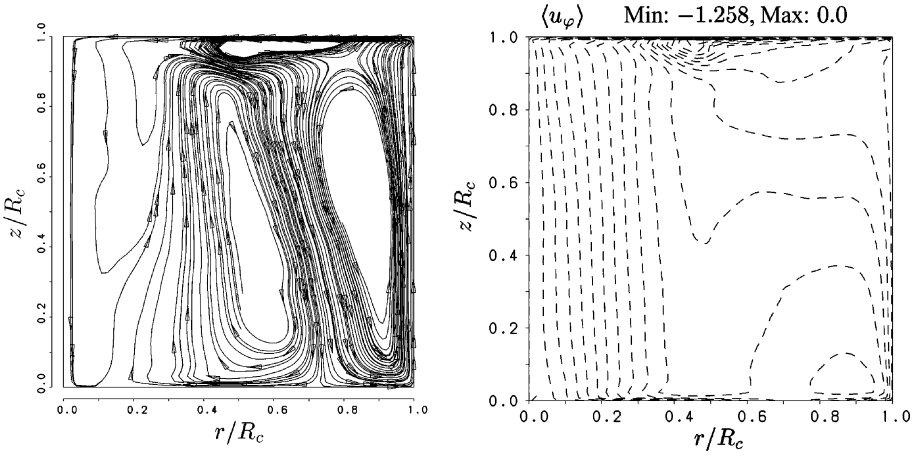

Fig. 9. Streamlines of the mean velocity fields (left) and contours of the circumferential velocity component (right) projected into (z, r)-planes of DNS_3 (low crystal rotation). Solid/dashed lines represent positive/negative values.

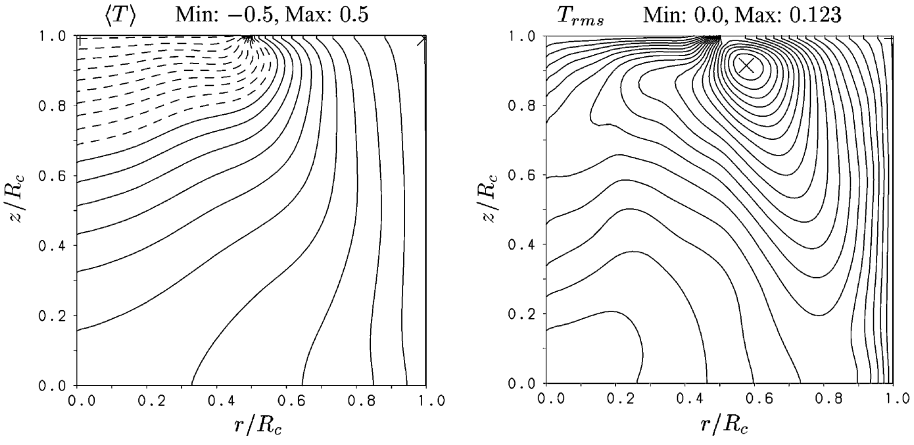

Fig. 10. Mean (left) and rms-values (right) of isotherms obtained in DNS_3 (low crystal rotation). Solid/dashed lines represent positive/negative values.

of the circumferential velocity component reflect a difference in flow structure, with horizontally oriented contours in parts of the melt underneath the free surface. In this region the buoyancy driven recirculation zone transports melt with a comparably low angular momentum from the crucible bottom towards the free surface.

A strong change in the flow structure due to the high crystal rotation rate is visible in Fig. 11 (DNS_4). A single recirculation zone dominates the mean flow in the (z, r)-plane, while two smaller cells are observed close to the upper part of the crucible wall and below the free surface. Additionally, due to the increased rotation of the crystal, a small recirculation structure is created just

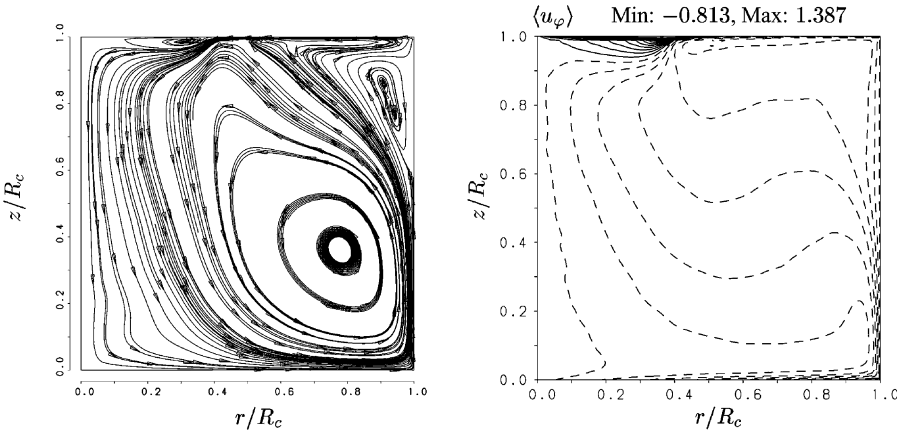

Fig. 11. Streamlines of the mean velocity fields (left) and contours of the circumferential velocity component (right) projected into (z, r)-planes of DNS_4 (high crystal rotation). Solid/dashed lines represent positive/negative values.

underneath the crystal. Therefore, mixing is enhanced within the crystallization zone leading to more uniform radial concentration gradients of impurities and dopants on the one hand. On the other hand this recirculation zone also acts as a trap for these substances. With this intense recirculation, melt with low angular momentum is mixed with the melt rotating at crucible rotation rates, which leads to curved contours of the circumferential velocity component in Fig. 11 (right). As indicated by the dashed isotherms in Fig. 12 (left) cold fluid extends over more than one half of the melt height, reflecting that the probability for undercooling of the melt is increased.

A shift towards the crucible bottom and axis of the position of maximum rms temperature fluctuation associated with an increased maximum value of $T_{\mathrm{rms}} = 0.181$ ($\approx$16.5 K) is reflected in Fig. 12 (right). Although temperature fluctuations of high amplitude are further increased for high crystal rotation rates, within the crystallization zone they are damped.

Increasing the Grashof number and the Marangoni number in DNS_5 does not significantly change the structure of the overall momentum and heat transport, as indicated in Figs. 13 and 14. Solely, the amplitude of maximum rms temperature fluctuations in Fig. 14 (right) increases, but its position remains.

Finally in DNS_6 and DNS_7, heat radiation at the free surface is taken into account assuming a background temperature of $T_{\mathrm{h}} = 1450$ K. While DNS_6 was performed for the Gr- and Ma-numbers of the reference case DNS_1, the Marangoni number was additionally reduced in DNS_7. Considering heat radiation, it has a remarkable effect on the radial heat flux close to the crystal edge as shown in Figs. 16 (left) and 18 (left). In contradiction to Fig. 5 (left) the isotherms are almost uniformly distributed along the free surface, reflecting the decreased radial heat flux at the crystal edge. Obviously, this also reduces the spatial resolution requirements, which are extremely high close to the crystal edge due to high temperature and velocity gradients, if heat

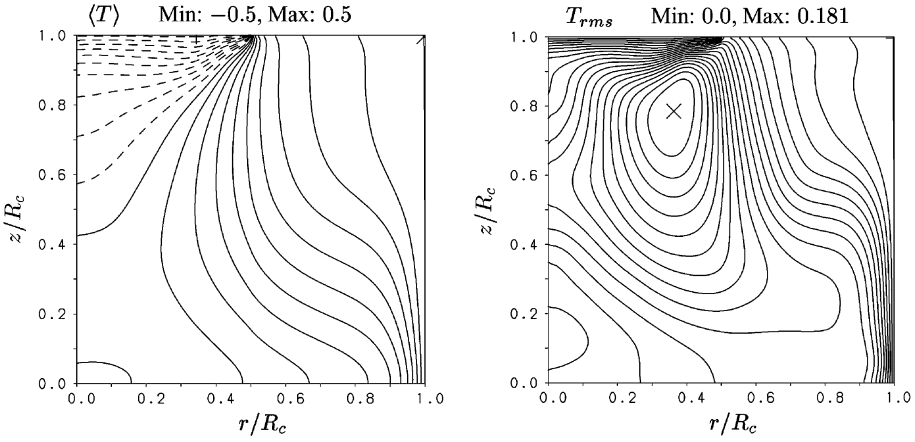

Fig. 12. Mean (left) and rms-values (right) of isotherms obtained in DNS_4 (high crystal rotation). Solid/dashed lines represent positive/negative values.

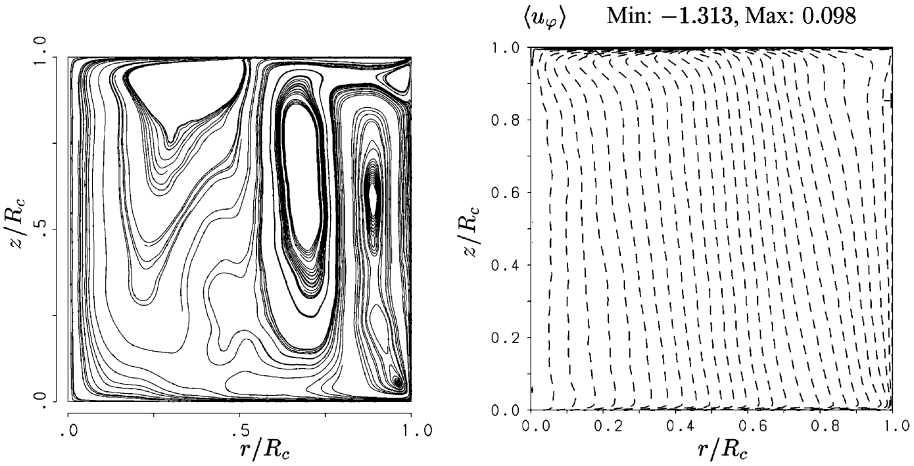

Fig. 13. Streamlines of the mean velocity fields (left) and contours of the circumferential velocity component (right) projected into (z, r)-planes of DNS_5 (high Grashof number). Solid/dashed lines represent positive/negative values.

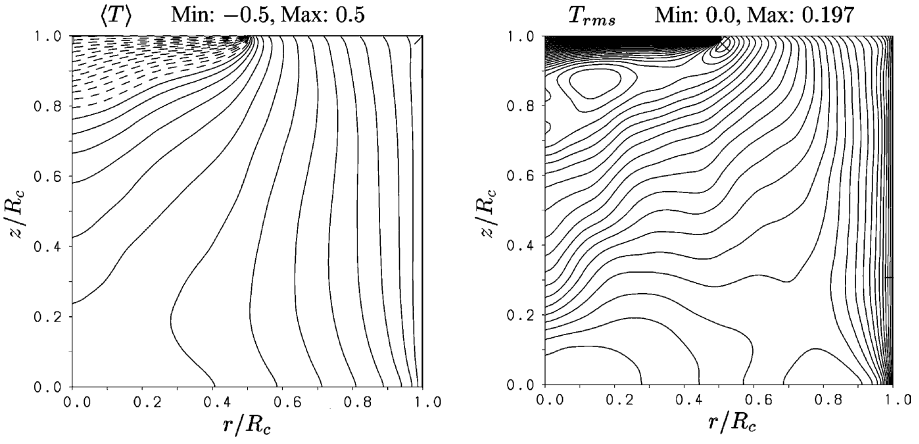

Fig. 14. Mean (left) and rms-values (right) of isotherms obtained in DNS_5 (high Grashof number). Solid/dashed lines represent positive/negative values.

radiation is neglected. Heat radiation also damps the radial momentum transport along the free surface and weakens the recirculation zone below the free surface in Fig. 15 (left). At the same time the three recirculation zones extend down all the way to the crucible bottom, which leads to the two characteristic regions for the circumferential velocity field, with vertical contours underneath the crystal and transversal contours below the free surface similar to those of Figs. 7 (right) and 9 (right). Additionally, reducing the Marangoni number also leads to these three recirculation zones, but a continuous flow in the boundary layer at the crucible bottom enhances mixing and leads to predominantly vertical contours of the circumferential velocity component as indicated in Fig. 17 (right). While the position of maximum rms temperature fluctuations is shifted away from the crystal edge with lower absolute values for DNS_6 in Fig. 16 (right), these values increase if the Ma-number is additionally decreased (see Fig. 18 (right)). For this case the position of maximum rms temperature fluctuations additionally moves away from the crystal edge towards the crucible axis.

4.5. Comparison between experiment and numerical simulation

DNS_8, the flow parameters of which are presented in Table 1, was conducted to compare computed temperature data to measurements, which were performed in a LEYBOLD EKZ 1300 crucible at Wacker Siltronic in Burghausen (Germany) (Wacker Siltronic, 2001). The same configuration was considered by Vizman et al. (2001) and Enger et al. (2001). In order to ensure comparability of the computation with this experiment, the wall temperature distributions for the DNS were interpolated from measured temperatures according to

$$T(z/R_c) = -4.6(z/R_c)^3 + 6.85(z/R_c)^2 - 3.615z/R_c + 0.5 \quad (9)$$

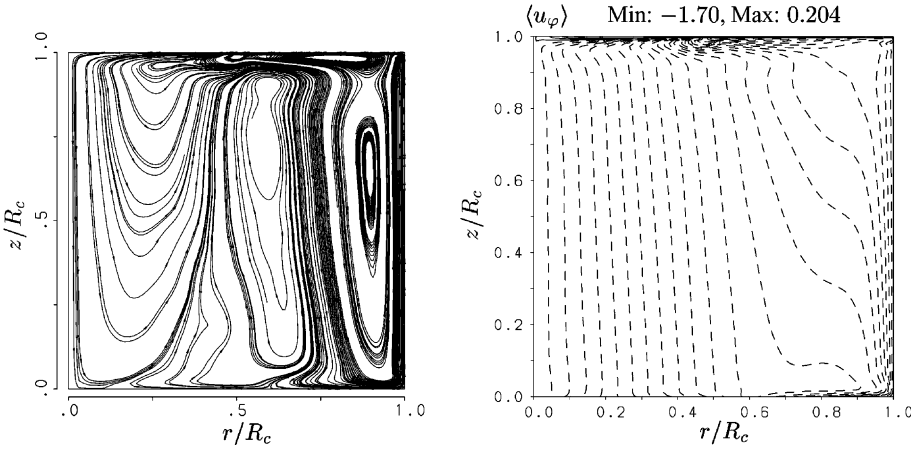

Fig. 15. Streamlines of the mean velocity fields (left) and contours of the circumferential velocity component (right) projected into (z, r)-planes of DNS_6 (heat radiation considered). Solid/dashed lines represent positive/negative values.

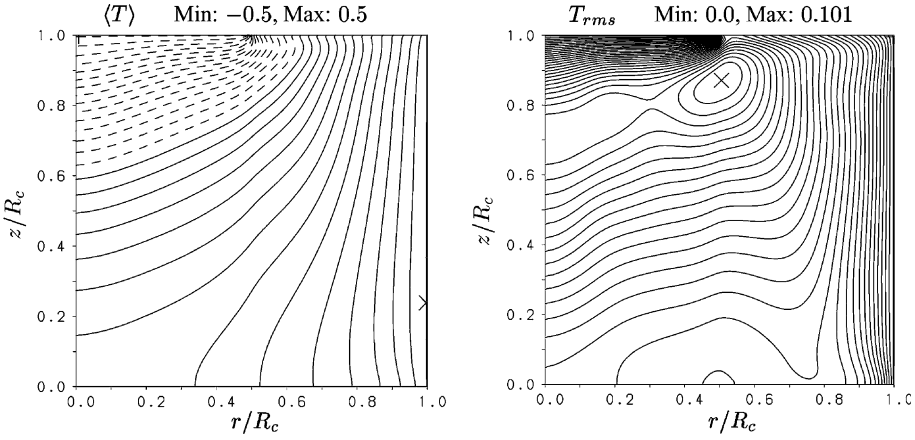

Fig. 16. Mean (left) and rms-values (right) of isotherms obtained in DNS_6 (heat radiation considered). Solid/dashed lines represent positive/negative values.

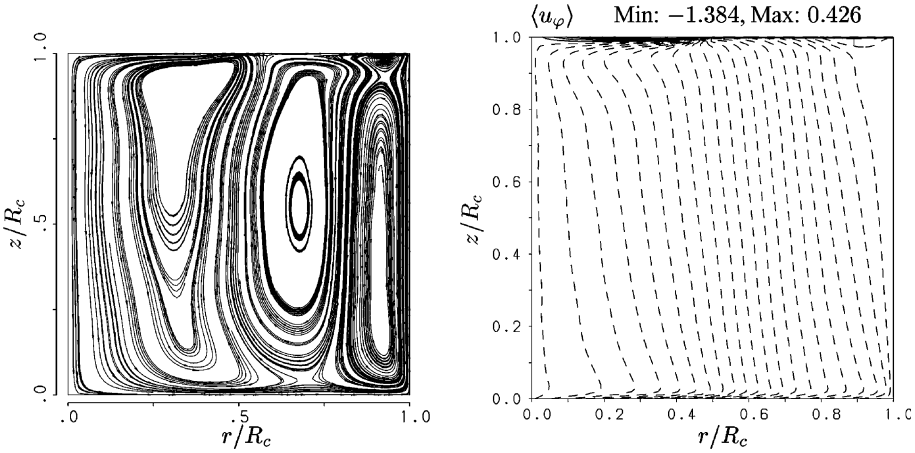

Fig. 17. Streamlines of the mean velocity fields (left) and contours of the circumferential velocity component (right) projected into (z, r)-planes of DNS_7 (low *Ma* number). Solid/dashed lines represent positive/negative values.

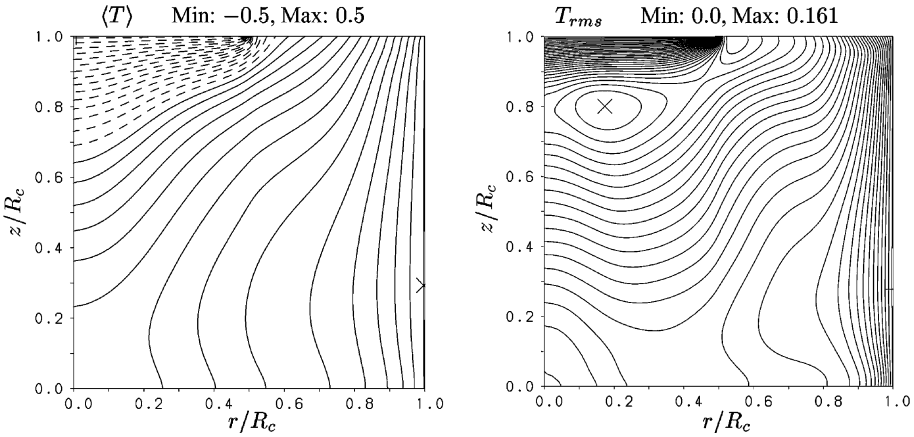

Fig. 18. Mean (left) and rms-values (right) of isotherms obtained in DNS_7 (low *Ma* number). Solid/dashed lines represent positive/negative values.

$$T(r/R_c) = 0.619(r/R_c)^2 - 0.119 \quad (10)$$

Additionally, heat radiation at the free surface was modelled using two different background temperature values, $T_h = 1510$ K for 5 cm $\leqslant r \leqslant$ 10 cm and $T_h = 1560$ K between $r = 10$ cm and $r = 17$ cm (crucible side wall).

The computed streamlines of the mean velocity fields are presented in Fig. 19. They indicate a flow, which is characterized by five major recirculation zones. The mean isotherms shown in Fig. 20 reveal a predominantly transversal orientation, for which the region of cold melt is increased. Contours of the rms temperature fluctuations demonstrate the existence of two characteristic regions of temperature fluctuations, one below the free surface with maximum values which are low compared to those in Fig. 5, and the other one below the crystal, where the contours are alligned with the crystal/melt interface.

The comparison of computed and measured values of mean temperature and rms temperature fluctuations for 6 different positions within the melt is presented in Table 2. The mean temperature values reveal differences of less than 6% of the overall mean temperature difference ΔT. This underlines, that although the Czochralski process was idealized to some extent, the simulations produce reliable results. Somewhere higher differences for the

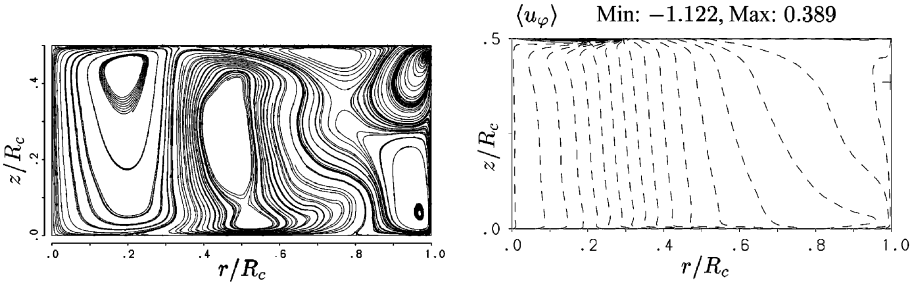

Fig. 19. Streamlines of the mean velocity field (left) and contours of the circumferential velocity component (right) of DNS_8. Solid/dashed contour lines represent positive/negative values.

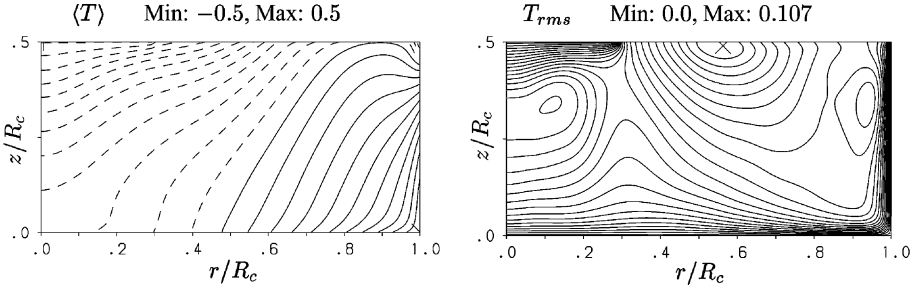

Fig. 20. Isotherms of the mean temperature (left) and of the rms fluctuating temperature (right) of DNS_8. Solid/dashed contour lines represent positive/negative values.

Table 2
Comparison of measured and computed mean temperatures and rms temperature fluctuations

$z/R_c, r/R_c$	0.44, 0.24	0.32, 0.24	0.21, 0.24	0.44, 0.43	0.32, 0.43	0.21, 0.43
$\langle T\rangle_{num}$	−0.33	−0.19	−0.13	−0.248	−0.121	−0.059
$\langle T\rangle_{exp}$	−0.30	−0.22	−0.17	−0.279	−0.176	−0.113
$T_{rms,num}$	0.047	0.058	0.051	0.081	0.064	0.053
$T_{rms,exp}$	0.037	0.045	0.0395	0.034	0.047	0.042

rms temperature fluctuations are found. To understand this, it must be noted, that the thermocouples used for the measurements in the hot Si-melt do not capture high frequency temperature fluctuations. This might be the reason, why the measured rms temperature fluctuations are low compared to the simulation data for all locations depicted in Table 2.

5. Conclusions

Direct Numerical Simulations of the turbulent flow in an idealized Czochralski crystal growth configuration have been performed for two melt heights, for different rotation rates of the crystal and crucible and for varying Marangoni and Grashof numbers.

While subjected to rotation by the crucible, the fluid is driven up the heated side wall by buoyancy and forced towards the crystal at the meniscus. From there surface-tension drives the flow towards the crystal edge, where it encounters the centrifugally forced flow from underneath the crystal. The positions of maximum rms temperature and velocity fluctuations are located within the crystallization zone just underneath the crystal edge.

Decreasing either the melt height, the rotation rate of the crystal or changing the Grashof and/or Marangoni number leads to minor changes in the bulk flow structure. Especially for low melt heights an increased influence of cold fluid increases the possibility of undercooling of the melt underneath the crystal, while rms temperature fluctuations decrease slightly.

Strong changes in the bulk flow structure are observed for high rotation rates of the crystal. The increased centrifugal forces underneath the crystal drive one major recirculation zone. Maximum rms temperature fluctuations increase with the rotation rate of the crystal. The position of maximum values moves towards the crucible bottom for DNS_4 (high crystal rotation rate). This shifted position of maximum rms temperature fluctuations, which is also observed if heat radiation is modelled and the Marangoni number is decreased, might lead to more friendly crystal growth conditions. The trade-off probably is a reduced mixing underneath the crystal, where impurities and dopant might be trapped in a small recirculation zone.

Good agreement of mean temperatures, which differed by less than 6%, was obtained in a comparison of computed and measured temperatures. This underlines that geometric idealization of the industrial Czochralski process is justified.

References

Bottaro, A., Zebib, A., 1989. Three-dimensional thermal convection in Czochralski melt. J. Cryst. Growth 97, 50–58.

Enger, S., Gräbner, O., Müller, G., Breuer, M., Durst, F., 2001. Comparison of measurements and numerical simulations of convection on Czochralski crystal growth of silicon. J. Cryst. Growth 230, 135–142.

Grötzbach, G., 1983. Spatial resolution requirements for direct numerical simulation of the Rayleigh–Bénard convection. J. Comput. Phys. 49, 241–264.

Jones, A.D.W., 1989. Flow in a model Czochralski oxide melt. J. Cryst. Growth 94, 421–432.

Kuroda, E., Kozuka, H., Takana, Y., 1982. Influence of growth conditions on melt interface temperature oscillations in silicon Czochralski growth. J. Cryst. Growth 68, 613.

Lai, Y.G., So, R.M.C., 1990. Near-wall modeling of turbulent fluxes. Int. J. Heat Mass Transfer 33, 1429–1440.

LeRibault, C., Friedrich, R., 1997. Investigation of transport equations for heat fluxes in compressible flows. Int. J. Heat Mass Transfer 40, 2721–2738.

Mihelcic, M., Wingerath, K., Pirron, Chr., 1984. Three-dimensional simulations of the Czochralski bulk flow. J. Cryst. Growth 69, 473–488.

Schumann, U., 1973. Ein Verfahren zur direkten numerischen Simulation turbulenter Strömungen in Platten- und Ringspaltkanälen und über seine Anwendung zur Untersuchung von Turbulenzmodellen. Dissertation, University of Karlsruhe.

Vizman, D., Gräbner, O., Müller, G., 2001. Three-dimensional numerical simulation of thermal convection in an industrial Czochralski melt: comparison to experimental results. J. Cryst. Growth 233, 687–698.

Wacker Siltronic GmbH, 2001. Private communication.

Wagner, C., Friedrich, R., Narayanan, R., 1994. Comments on the numerical investigation of Rayleigh and Marangoni convection in a vertical circular cylinder. Phys. Fluids 6 (4), 1425–1433.

Wilcox, W.R., Fullmer, L.D., 1965. Turbulent free convection in Czochraski crystal growth. J. Appl. Phys. 36 (7), 2201–2206.

Xiao, Q., Derby, J.J., 1995. Three-Dimensional melt flows in Czochralsky oxide growth: high-resolution, massively parallel, finite element computations. J. Cryst. Growth 152, 169–181.